Determining thin film roughness with EUV reflection

Cody L. Petrie

A senior thesis submitted to the faculty of
Brigham Young University
in partial fulfillment of the requirements for the degree of

Bachelor of Science

R. Steven Turley, Advisor

Department of Physics and Astronomy

Brigham Young University

August 2014

Copyright © 2014 Cody L. Petrie

All Rights Reserved

ABSTRACT

Determining thin film roughness with EUV reflection

Cody L. Petrie
Department of Physics and Astronomy
Bachelor of Science

We have developed a method to measure the roughness of thin films using extreme ultraviolet (EUV) light. This method is more sensitive to roughness with characteristic features on the length scale of a wavelength of light (a few nm) than existing methods like atomic force microscopy (AFM). We have used EUV reflection, geometrical optics (GO), and physical optics (PO) calculations to determine the roughness of UO_x thin films. The two samples we have used had thicknesses of 44 and 412 nm respectively. We have generated random rough surface models and used PO to calculate the reflection that we should see from these surfaces. These calculations were compared to reflection measurements taken on each sample at the Advanced Light Source to determine the roughness of each sample. We were not able to fit PO calculations to the 44 nm data, but were able to get some insight into the topography of the surface with GO. Four measurements were taken on the 412 nm sample at different incident angles and with different wavelengths of EUV light. We modeled the surface with the rms roughness height and the width of the Gaussian packet of spatial frequencies. We determined the rms height to be 0.78±0.15 nm and the width of the Gaussian packet to be $8.3\times10^{-5}\pm2.7\times10^{-5}$ nm^{-1}. For the 412 nm sample the AFM determined the rms roughness heights to be 9.39 nm. This shows that our method has potential to provide more resolution than AFM in measuring surface roughness. This also demonstrates that optical techniques provide a potential means for measuring roughness when other methods are inaccurate.

Keywords: extreme ultraviolet, EUV, XUV, thin film, surface roughness, geometrical optics, physical optics

ACKNOWLEDGMENTS

I would like to thank my wonderful wife for her love and support. Through the exciting moments and the frustrating days both, she has always been there for me. I would also like to thank my parents for their love and support. I would never have had the courage to go to college and study physics without them. My adviser Dr. Steven Turley has provided me with the time, lessons, and encouragement that I have needed to make it through my undergraduate degree. I am also grateful to Dr. David Allred for his insights, and for making the thin films that were used to take my measurements. Eric Gullikson manages beamline 6.3.2 at the ALS, and has provided me with the tools needed to take reflection measurements on our thin films. I would like to thank the BYU physics department for providing me with the means to accomplish this work, especially for the REU program which provided me the opportunity to begin doing research. The ORCA program has also provided me with the opportunity to continue working on this project while going through school and raising a family.

Contents

Table of Contents **iv**

List of Figures **v**

1 Introduction **1**
1.1 Extreme Ultraviolet Light . . . 1
1.2 Thin Film Roughness . . . 3
1.3 Existing Roughness Measurements . . . 4
1.4 Determining Roughness . . . 6
1.5 Roughness Calculations . . . 7

2 Methods **12**
2.1 Thin Films . . . 12
2.2 Reflection Measurements . . . 13
2.3 AFM Measurements . . . 16
2.4 Computational Methods . . . 18

3 Results **23**
3.1 Reflection . . . 23
3.2 Understanding Surface Roughness . . . 23
3.3 Comparison to AFM . . . 30

4 Conclusion **31**
4.1 Conclusion . . . 31
4.2 Future Work . . . 32

Bibliography **33**

Index **36**

List of Figures

1.1 Plane wave reflected from both smooth and rough surfaces. 2
1.2 Two different surfaces with different rms heights and different spatial frequency distributions. 4
1.3 Reflection from a multilayer thin film 4
1.4 Schematic of the AFM. 5
1.5 Calculation showing the weakness of AFM resolution. 5
1.6 Two different surfaces with the same rms height. 8
1.7 Example reflection calculations done with GO. 9

2.1 Schematic of the sputtering chamber. 14
2.2 Schematic of beamline 6.3.2 at the ALS. 15
2.3 Schematic of the reflectometer at the ALS. 16
2.4 AFM data. 17
2.5 Characteristic Gaussian envelope for a model surface. 18
2.6 Process of creating model surfaces from random Gaussian noise. 21
2.7 Geometry used to derive the Fresnel coefficients. 22
2.8 Calculations comparing reflection with an incident plane wave and an incident Gaussian beam. 22

3.1 412 nm reflection data. 24
3.2 44 nm reflection data. 25
3.3 Fits to 412 nm reflection data. 27
3.4 Characteristic curve predicted by GO. 29
3.5 Maximum angle of reflection for 44 nm thin film. 29

Chapter 1

Introduction

1.1 Extreme Ultraviolet Light

Extreme ultraviolet (EUV) light has wavelengths between 1-100 nm. Possessing a large imaginary part of the index of refraction for most materials, EUV light is absorbed strongly in most materials. For this reason it has not been studied as extensively as the light in other areas of the electromagnetic spectrum. As a result, there is great potential to learn new things and find new applications to EUV light.

One of the applications that our group has worked on is astronomical research. In March of 2000 the IMAGE mission was launched to study how He^+ is distributed in Earth's magnetosphere [1]. An important transition for He^+ is the 30.4 nm lines, and thus effective EUV mirrors were required for this mission. Our group helped design and build the mirrors that were used to image the Earth's magnetosphere.

Another application to EUV light is lithography. Lithography is commonly used to fabricate integrated circuits. The ability to make smaller circuits depends on the ability to use light with smaller wavelengths. EUV light can provide more resolution than visible or ultraviolet light.

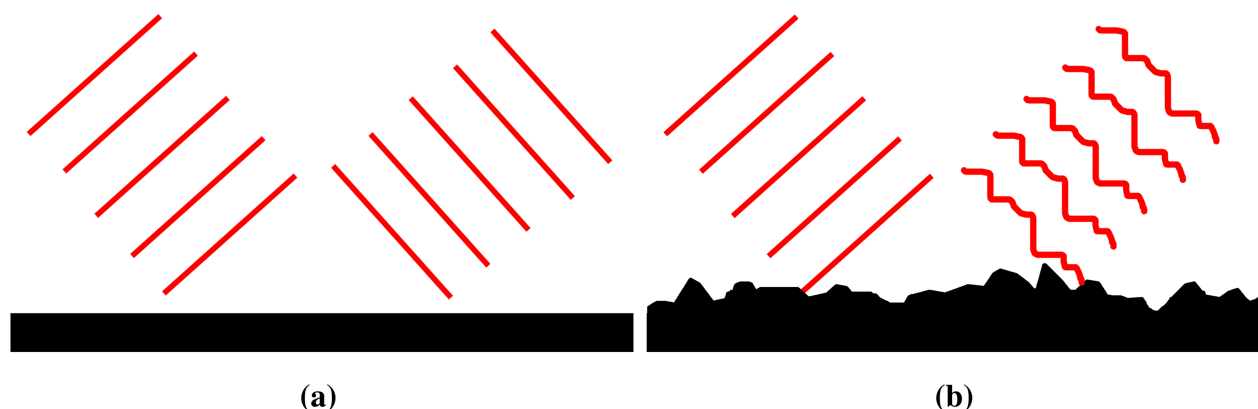

Figure 1.1 Figure 1.1a is a plane wave representation of perfect specular reflection while Figure 1.1b shows the effects of roughness on reflection. This roughness causes the beam to spread out in the far field. Due to the small wavelength of EUV light a surface may scatter light, such as in 1.1b, while to visible light the surface may look smooth like in 1.1a.

Christian Wagner *et al*. explain how EUV lithography would be an improvement to the lithography we use today [2]. But EUV lithography requires new advancements in EUV optics.

EUV light can also be used as a tool for microscopy. Microscopy is the field of using tools to look at things that we could otherwise not see with our eyes. We have used EUV light to probe surface roughness of thin films. The smaller the wavelength of light the more resolution that it has for microscopy. This is illustrated in Figure 1.1. Since the wavelength of EUV light is on the order of 1-100 nm it could give us a resolution of 10-1000 atoms on the surface of a thin film. This resolution is necessary to see roughness on our thin films. In addition, these measurements are being used to aid in making EUV optics, and thus EUV light is by definition able to probe any roughness that we need to see.

Other fields such as medicine and plasma diagnostics, particularly in stellar observations [3], could use EUV light as a tool to advance their fields. However to advance any field with EUV light we must first understand how to better use EUV light. Since it does not reflect strongly from most surfaces we need to make reflecting surfaces as smooth as possible in order to get the largest flux

of reflected light. To be able to make smooth optics we need to be able to characterize how smooth they are on the scale of EUV wavelengths.

1.2 Thin Film Roughness

We chose to use two parameters to make generalized, qualitative descriptions of rough surfaces. The first parameter is the rms roughness height. This is the average deviation of the surface relative to a flat surface. The rms height is given by

$$h_{\text{rms}} = \sqrt{\frac{1}{n-1}\sum_i (h_i - \bar{h})^2}, \tag{1.1}$$

where h_{rms} is the rms height, n is the number of surface points, h_i corresponds to points on the surface, and $\bar{h}$ is the mean height. The second parameter is the spatial frequency power spectral distribution of the roughness on the surface. A good way to control this parameter for model surfaces is by filtering the surface in frequency space with a Gaussian filter. Figure 1.2 shows the difference between these two types of measurements. In Figure 1.2a the surface has a greater rms roughness height and spatial frequency than the surface in Figure 1.2b. Each of these parameters causes reflection from the surface to change.

Because EUV light does not reflect well from most material surfaces, multilayer thin films are used to create a reflecting surface. Multilayer mirrors are designed such that the interlayer spacing will create a coherent addition of the reflected waves, thus optimizing the amount of light you get from reflection. However, each underlying layer adds to the roughness of the sample which is hard to model. We have only done calculations and measurements on single layer thin films to keep the model simple. Figure 1.3 illustrates reflection for an ideal multilayer surface. In reality each layer would have its own roughness. This is called correlated roughness. In reality multilayers have a mix of correlated and uncorrelated roughness. D.E. Savage *et al.* discuss the more complicated multilayer model with correlated roughness [4].

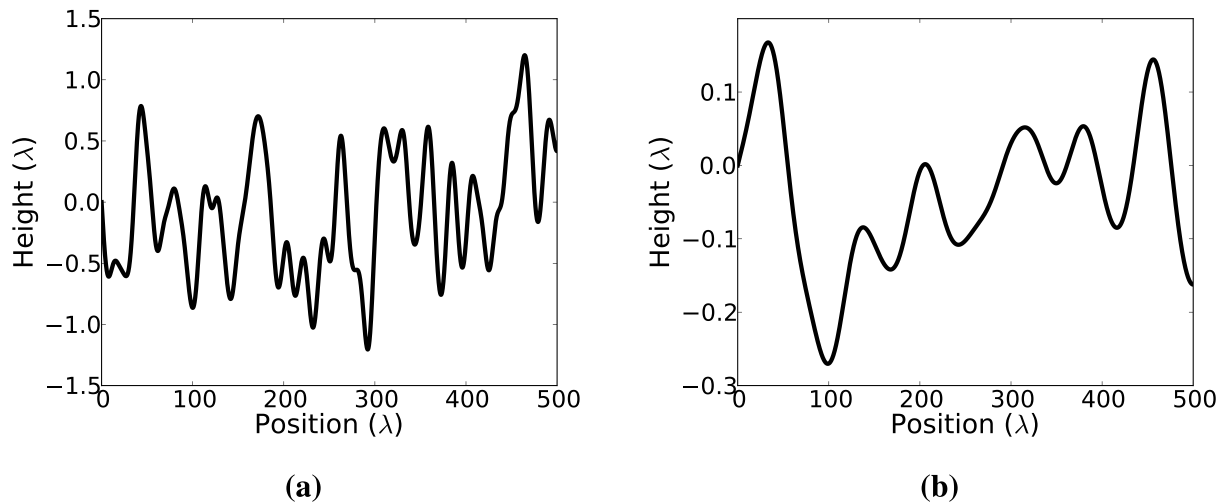

Figure 1.2 The rms height and spatial frequency in surface 1.2a are both greater than those of surface 1.2b. The scales for the height and position are both in terms of the wavelength of light.

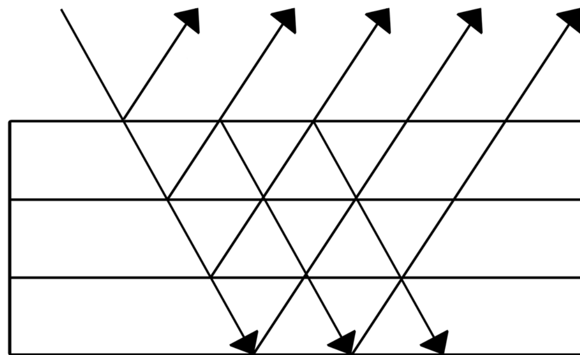

Figure 1.3 Reflection from an ideal multilayer thin film surface. Notice how each layer contributes to the total reflection.

1.3 Existing Roughness Measurements

Atomic force microscopy (AFM) is currently the best way to measure the roughness for our samples. The AFM consists of a cantilever with a tip on the end. The tip is dragged or tapped across the surface. As it moves across the surface a laser is reflected from the end of the cantilever. As the tip moves up and down with the surface, the movement is measured from the reflected laser.

An illustration of the cantilever, tip and laser is shown in Figure 1.4. The problem with this type

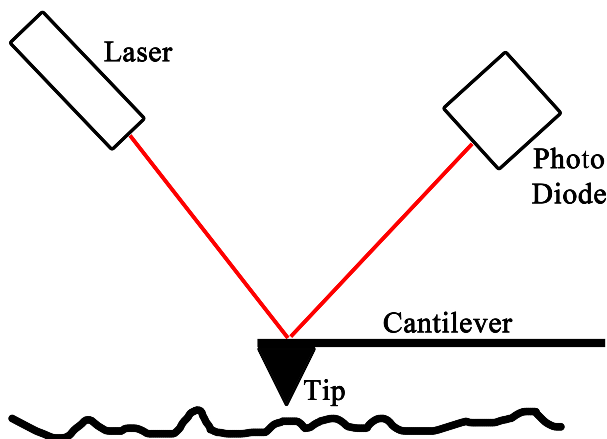

Figure 1.4 Setup of the AFM. The tip is moved across the surface and a laser is reflected from the end of the cantilever to measure the movements of the tip.

of measurement is that it depends on having tips smaller than the roughness features of the sample to be measured (see K.L. Westra *et al.* for a review [5]). Figure 1.5 shows the problems you have when trying to use an AFM to measure roughness on the nm scale. To help us build better optics for EUV light we need a better probe than the AFM.

Surface roughness can also be measured by electron microscopy. Electron microscopy comes in two forms, scanning electron microscopy (SEM) and transmission electron microscopy (TEM).

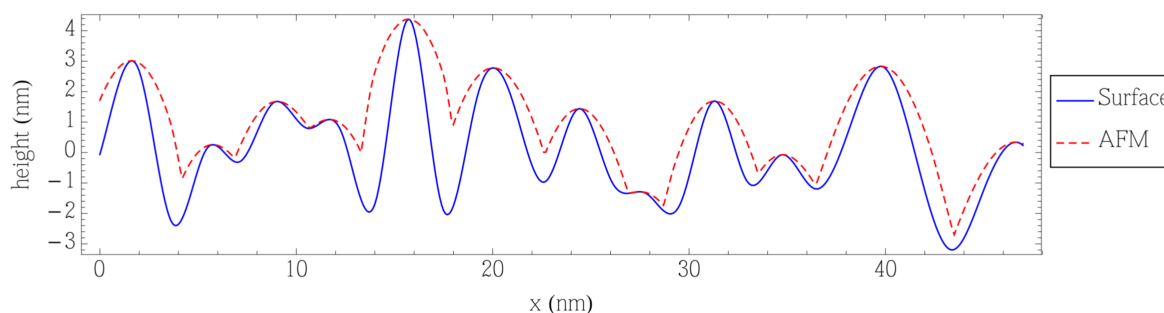

Figure 1.5 When the tip of an AFM is larger than the characteristic roughness of a surface the AFM is unable to detect all of the roughness. This example was with done with a parabolic tip with radius of 3 nm. The actual rms roughness was 1.50 nm and the measured roughness was 0.76 nm.

Both of these methods are impractical to use to measure the roughness of our films. The SEM does not have the resolution that we need and the process of preparing TEM samples generally alters the surface characteristics. To prepare a sample for the TEM you need a slice of the sample such that an electron beam can pass through. It is difficult for us to get good roughness measurements from either of these methods.

1.4 Determining Roughness

We have taken reflection measurements on two UO_x thin films. Each of these thin films was sputtered on a smooth $Si/Si0_2$ substrate and has a different roughness. We have measured the roughness of these thin films using AFM so that we can compare our results to the current methods of measurement. Each of the reflection measurements has been compared with calculations of reflection for a rough model surface. We have determined the roughness of our thin films by matching the reflection of the real surface to the calculated reflection of the model surface whose roughness parameters are known. This allows us to determine multiple roughness parameters. The two parameters that have been varied in our model surfaces are rms roughness and the distribution of spatial frequencies. Reflection is sensitive to roughness that is comparable to, and larger than, the wavelength of light. This means that by using EUV light we can probe surface roughness that is on the scale of 1-100 nm.

Previous students [6, 7] in our group have estimated roughness based on a method similar to those of Debye-Waller and Nevot-Croce [8–10]. These methods use the reflectance of a surface to determine the roughness. They also model the roughness on the surface with only the rms roughness height and ignore any spatial distribution of the roughness. The Debye-Waller and Nevot-Croce factors are

$$\frac{R}{R_0} = e^{-4q^2h^2} \tag{1.2}$$

and

$$\frac{R}{R_0} = e^{-4q_1q_2h^2} \tag{1.3}$$

respectively, where $\frac{R}{R_0}$ is the ratio of peak reflected light from a rough surface to a smooth surface, h is the rms roughness, and q is the momentum that is perpendicular to the flat surface. The Nevot-Croce factor finds q for both the top and bottom of the surface whereas the Debye-Waller factor just calculated one q. The momentum can be given by

$$q = \frac{2\pi\mathscr{N}}{\lambda_0}\sin\theta_i \tag{1.4}$$

where $\mathscr{N}$ is the index of refraction, λ_0 is the wavelength of light, and θ_i is the angle of incidence. From these factors the rms roughness can be solved for when the ratio of reflected light for rough and smooth samples is known. As mentioned above, these methods leave out the spatial frequency of the roughness. Hart developed a correction factor similar to these in [7]. Equation 1.5 shows Hart's factor which includes a linear and cubic term in the factor.

$$\frac{R}{R_0} = e^{0.28qh-3.58(qh)^2+0.87(qh)^3} \tag{1.5}$$

Both of these methods model surface roughness using only the rms roughness height. Two very different surfaces can have the same rms roughness height as illustrated in Figure 1.6. The method used in this thesis includes more than just the specular reflection to determine the roughness of a thin film and uses a model of roughness that includes the spatial distribution of the roughness.

1.5 Roughness Calculations

There are three methods that we have used to calculate EUV reflection. The first of these is geometrical optics (GO), or ray optics. We have used GO to model the long wavelength features of surface roughness. The advantage to GO is that it is a simple and quick calculation. In ray optics, light is treated as a set of rays that point in the direction that light is traveling. Reflection is easy to

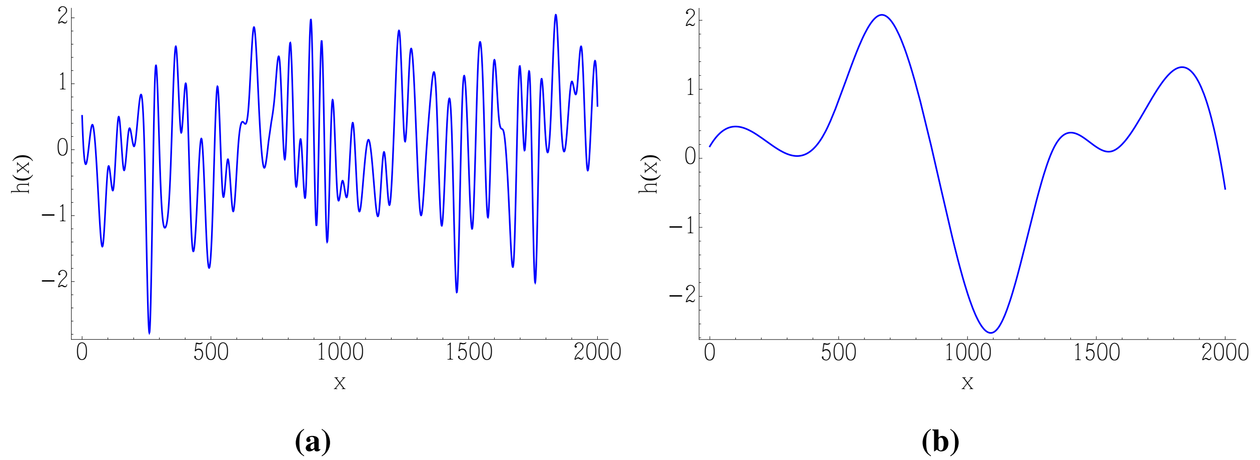

Figure 1.6 Two different surfaces, both with rms roughness of 1 (arbitrary units). Despite having the same rms height the surfaces are very different. This is why we model surface roughness with rms height and distribution of spatial frequencies.

calculate from ray optics because each ray simply follows the law of reflection, which states that the angle between the incident ray and the interface is the same as the angle between the reflected ray and the interface. As a result, the only major calculation to do is the calculate the derivative at each point on the surface. The angle at which each ray will reflect is given by

$$\theta_{\text{ref}} = \arctan\left(\frac{-dh(x)}{dx}\right) + \theta_{\text{spec}} \tag{1.6}$$

where $h(x)$ is the function that describes the surface and θ_{spec} is the angle of the specular peak. Two GO calculations, on a flat and rough surface respectively are shown in Figure 1.7. Notice that from a flat surface GO predicts that all of the reflection will be at a single angle, the specular angle. Diffraction and shadowing effects are not taken into account when doing GO. For this reason we generally only used GO to get a preliminary understanding of reflection for surfaces. As will be shown later, GO was used to gain an understanding of reflection for surfaces that had large-scale, where the features are much larger than the wavelength of light, bumps or pillows on the surface.

Physical Optics (PO) is a more difficult yet more accurate representation of reflection. We have used PO to model the short wavelength features of surface roughness. Unlike GO, diffraction

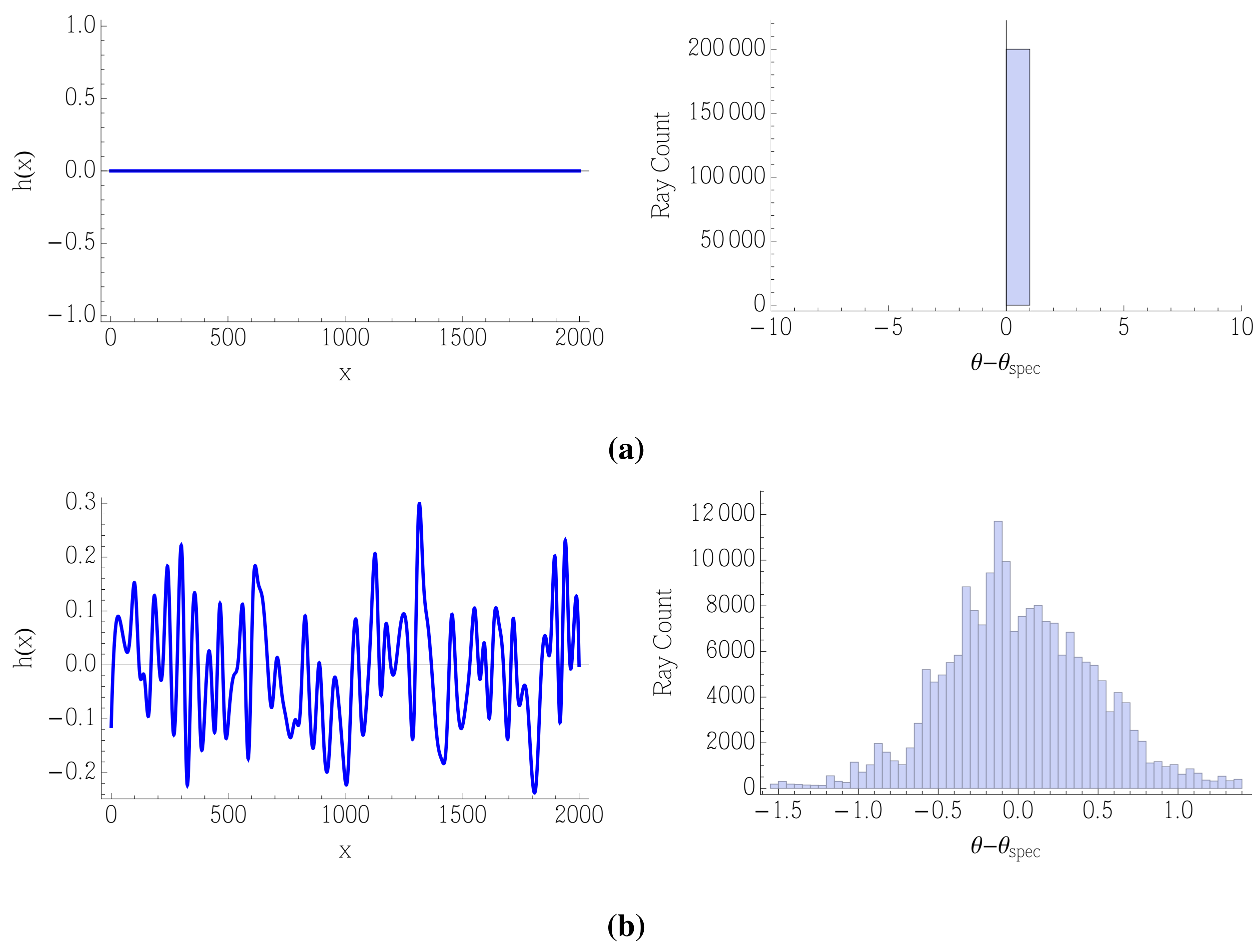

Figure 1.7 Plotted surfaces(left) with histograms (right) of GO calculations on flat and rough surfaces respectively. The x axis is the angle of reflection minus the specular angle.

effects are taken into account by PO. There are two parts to PO. First, Maxwell's equations are written in terms of surface parameters. With a known incident beam these equations can be used to solve for the surface currents. To solve for these currents it is assumed that the surface is locally planar. This is the Kirchhoff approximation which assumes that the surface height changes slowly over distances that are large compared to the wavelength, allowing us to assume that the surface is locally flat. Second, these currents are used as equivalent sources for Maxwell's equations to solve for the radiated fields. The equations of PO are quoted in section 2.4. The accuracy of this method increases as the surface roughness decreases. Since we are wanting to measure surface roughness, we would like to use this method on surfaces with a variety of surface roughness. A more exact solution would be preferable.

The final method we have used is a numerical solution to boundary element equations derived from Maxwell's equations. This solution is exact but takes more time than PO. My work has all been done with PO calculations. Johnson has compared PO with the exact solutions and has shown that for surfaces similar to ours PO is not a good approximation [11]. Despite its weaknesses PO is much faster than the method of solving Maxwell's equations directly. For this reason we have used PO to get some initial results. Our PO calculations were done on dielectric materials and should be more accurate than Johnson's calculations on perfect conductors. Other methods for calculating reflection can be found in [12] and [13]. In [12], Stearns comes up with an analytical expression for near and far field scattering, using the first Born approximation, which assumes that the scattered field is weak. This is a limitation that is not acceptable for our purposes since we are trying to optimize the amount of light scattered. Thus, our approach does not make the assumption of weak scattering but allows for stronger scattering.

Sinha [14] and Gullikson [15] both used the first Born approximation in their calculations of scattering. Gullikson uses surface profiles to determine the effects roughness has on scattering from rough surfaces. Sinha moves past the first Born approximation by using the distorted-wave

Born approximation, a perturbation method that adds perturbations to reflection from a flat surface, to explore the region of strong reflection.

We have used a PO calculation to determine the roughness of thin films. These calculations have been compared with the reflection measurements taken at the Advanced Light Source (ALS). We varied the parameters of the model surface until the calculated reflection agreed with the measurement. When the reflection profiles agreed the roughness of the sample matches the roughness of the model surface.

Chapter 2

Methods

2.1 Thin Films

We sputtered two single layer UO_x thin films on smooth Si/$Si0_2$ substrates with rms roughness of about 0.1 nm over area of 1 μm^2. We expect that these thin films are UO_3, however we have also seen evidence for UO_4 [16]. For this reason we call it UO_x. The thicknesses of the films were measured by ellipsometry to be 44.4±1.3 nm and 412.9±7.0 nm. Where 1.3 nm and 7.0 nm are the standard deviation of measurements taken at a variety of spots on the sample. Both of these thicknesses were fit using a model with fixed indices of refraction. Due to inaccuracy in the measurement and the fact that the exact measurement spot is unknown when we do reflectometry we don't know the exact thickness for our measurements. Each sample has different roughness so that we could compare our results for samples of varying roughness. In addition, the thickness and roughness of each sample vary across the sample. To account for this we take measurements on different parts of the surface. We used uranium films because uranium is one of the most reflective single layer materials in the EUV. Oxidation of the uranium is difficult to avoid, and thus we have done studies on UO_x. Sandberg discusses UO_x as a reflector for EUV applications [17].

We sputtered our thin films using DC magnetron sputtering (DCMS) . To do DCMS the vacuum chamber is pumped down to high vacuum. Once we are down at high vacuum, argon is introduced into the chamber. The DC bias creates an argon plasma. The argon ions are then confined to orbit above the uranium target by a magnet just behind the target. These ions will collide with the target launching uranium atoms in all directions. Some of these atoms will collide with the substrate and be bound to its surface forming a thin layer of uranium atoms. For the 44 nm film the base pressure was $\approx 1 \times 10^{-6}$ torr and the preplasma gas percentages were $\approx$60.56% O_2 and $\approx$39.33% Ar. For the 412nm film the base pressure was $\approx 8.0 \times 10^{-7}$ torr and the preplasma gas percentages were $\approx$49.39% O_2 and $\approx$50.06% Ar.

Bell discusses our specific setup and technique in detail [18]. A schematic of our sputter chamber can be seen in Figure 2.1.

2.2 Reflection Measurements

We took reflection measurements on two thin film samples at the Advanced Light Source (ALS) at Lawrence Berkeley National Laboratory. The ALS consists of a third-generation synchrotron. At the ALS electrons are accelerated in an inner ring (booster ring) until they are ready to enter the main ring where electrons are moving at fractions of a percent below the speed of light. These electrons are bent around the ring by magnets. As the electrons accelerate around the main ring they radiate in the form of photons. These photons have a variety of energies. There are different end stations, or beamlines, from which experiments utilize these radiated photons. We utilized the ALS to measure nonspecular reflection as a function of angle.

Our measurements were taken at beamline 6.3.2 which is dedicated to experiments involving EUV and soft x ray reflection and scattering experiments. There are a variety of optics and filters to collimate and filter the light to a chosen wavelength. There are also a number of filters that can

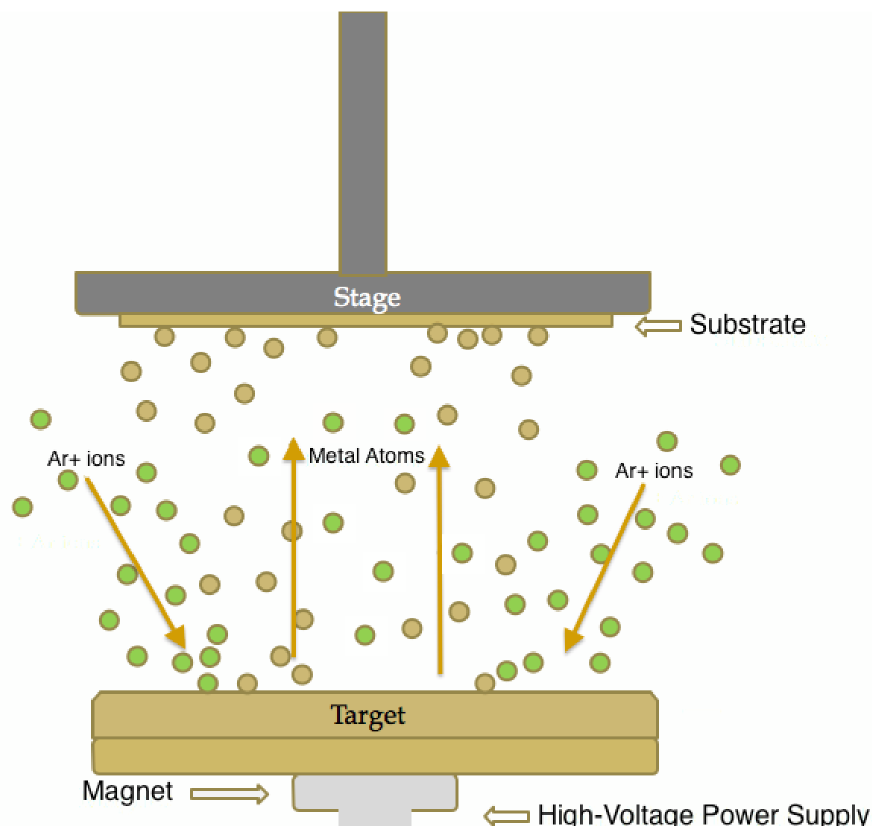

Figure 2.1 Schematic of the sputtering chamber.

be used to attenuate the light entering the chamber. A schematic of beamline 6.3.2 can be seem in Figure 2.2. We utilized both the photodiode and channeltron detectors. The photodiode was used to collect data on the reflectance per angle of each sample, and the channeltron was used to measure the nonspecular reflection. The energy range of the photons at 6.3.2 is 25-1300 eV which allowed us to take measurements at a number of different wavelengths. The spot size of the light at the sample is 150×50 μm where the 50 μm is in the direction of motion of the detector. Different size slits and circular apertures can be placed in front of the detector giving us better angular resolution. Filters can be used to set the wavelength with a precision of 0.007% with spectral purity of 99.98%. The light is 90% s polarized at our wavelengths. The detectors can be moved to within 0.01° and the sample can be moved in the x, y and z direction with a precision of 10 μm.

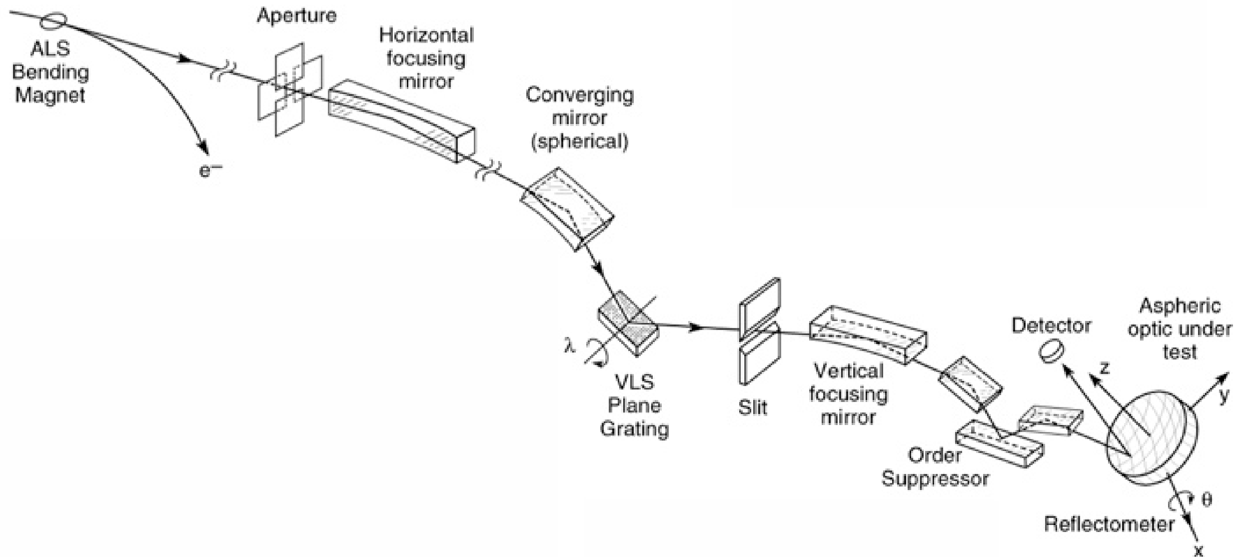

Figure 2.2 Schematic of beamline 6.3.2 at the ALS. The beam coming from the bending magnet is a broadband source which is focused through mirrors. A wavelength is then selected by a grating, the beam is narrowed by a slit and focused again by a mirror. Then the beam passes through an order sorter filter to increase the spectral purity before entering the vacuum chamber. This figure from [19].

The angular acceptance of the detector was 0.17° in the direction of the measurement and much larger in the transverse direction. Underwood *et al.* report more details about the construction and calibration of beamline 6.3.2 [20].

To take the measurements, the sample is set at an angle, which will be called θ, to the incident beam as shown in Figure 2.3. The incident beam is then reflected from the thin film into the detector. The detector can be swept over a variety of angles to measure the nonspecular reflection. We used the channeltron detector to measure the nonspecular reflection. Because the channeltron has an upper limit for the number of photons it can detect safely we started far from the reflection peak and scanned toward the peak. As the counts became too large we would stop, add a filter to decrease the number of photons in the beam, and then continue measuring, including overlap points between runs. We stitched the scans together by averaging the overlap measurements between each scan.

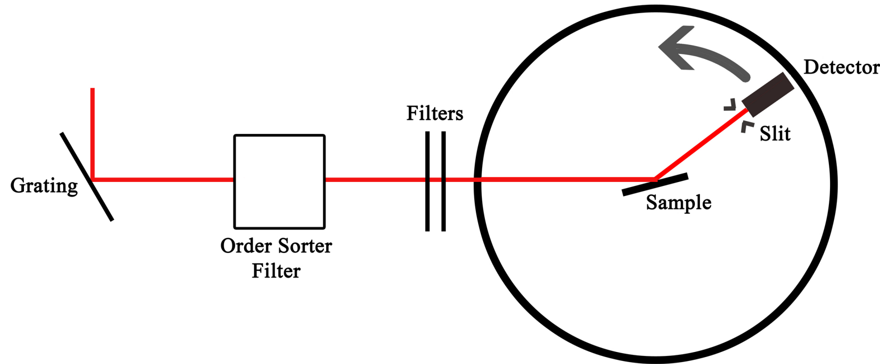

Figure 2.3 Schematic of the reflectometer at the ALS. The synchrotron radiation is coming from the left of the vacuum chamber.

Once the scans were stitched together we normalized the reflection to the ALS beam current and subtracted detector dark counts. The dark counts form the detector were a factor of around $10^5 - 10^6$ times smaller than our signal. To compare these measurements with the calculations done we normalized the measurements to have an integral of one over the range that we compared, using

$$I_{\text{norm}} = \frac{I}{\int_a^b I d\theta}, \tag{2.1}$$

where I_{norm} is the normalized reflection, I is the reflection, and a and b represent the range of angles that will be compared to calculations. We then match the peak of the calculated reflection to the measured reflection.

2.3 AFM Measurements

We have measured the roughness of each thin film on the AFM to compare with our reflection measurements. Although the roughness measurement has weaknesses, it provides us with a preliminary idea of how rough each sample is. The limitations of looking for small roughness with the AFM are illustrated in Figure 1.5. Westra *et al.* reported the affects that tip shapes and sizes have on roughness measurements [5]. The AFM reported a roughness of 9.39 nm and 16.8 for the

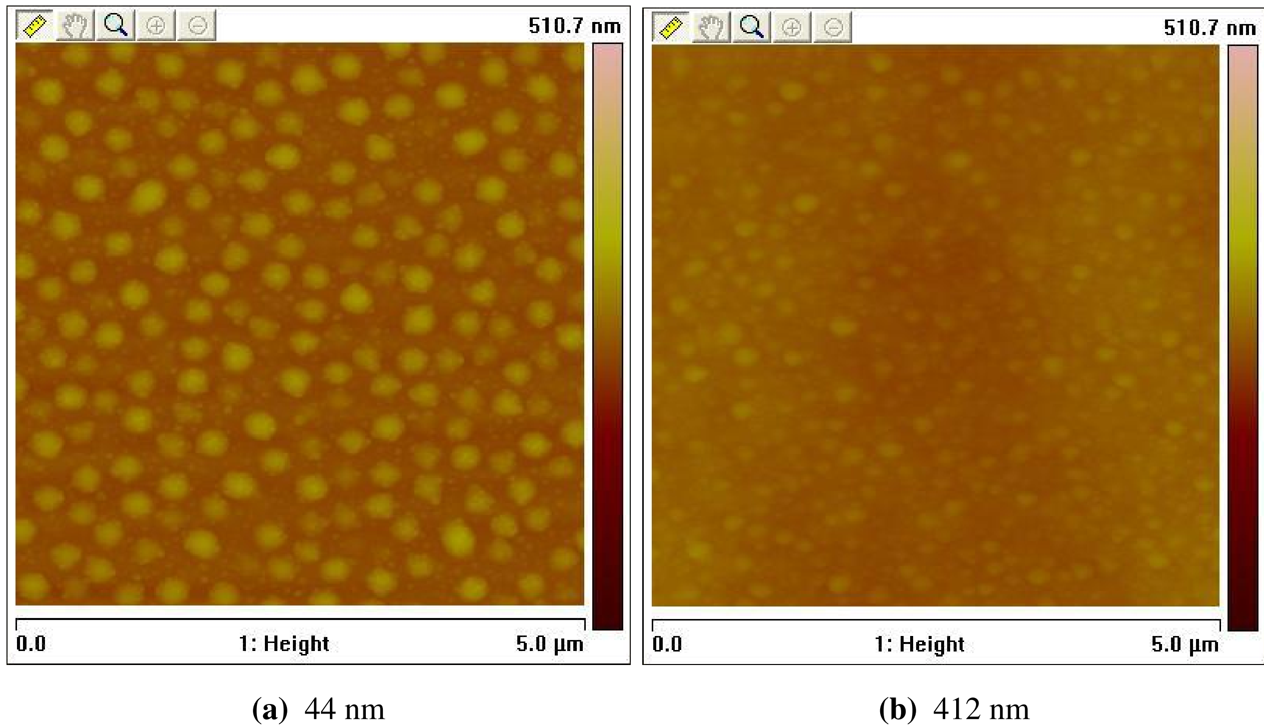

(a) 44 nm

(b) 412 nm

Figure 2.4 AFM scans of both samples. Notice the bumps that have formed on the surface of the 44 nm sample. These bumps may affect our reflection results.

412 nm and 44 nm samples respectively. The size of our tips are larger than that and so we have reason to believe that these measurements are inaccurate when trying to measure roughness on the wavelength scale of EUV light. Our reflection method can probe roughness that are much smaller than the AFM can.

AFM scans of both samples are shown in Figure 2.4. Notice the large bumps on the 44 nm sample. The size of the bumps is on the order of hundreds of nm, which is much larger than our wavelengths. We suspect that these bumps have affected our reflection measurements. However, by GO analysis we found that these bumps give a characteristic reflection profile and so we can learn about the bumps by reflecting light from the surface. This will be discussed in section 3.2.

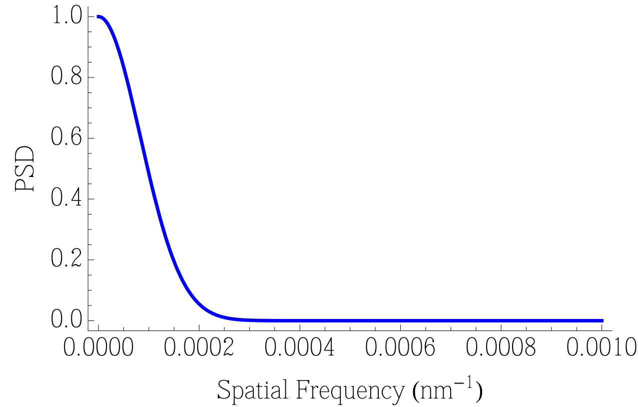

Figure 2.5 Characteristic Gaussian envelope used to generate the power spectral density for a model surface with Gaussian width of 8.30×10^{-5} nm^{-1}.

2.4 Computational Methods

We have done reflection calculations using geometrical optics (GO) as well as physical optics (PO). To do these calculations the surface is first generated as random Gaussian noise. This yields a surface with high spatial frequencies. To get rid of these high frequencies a Fourier transform was done to get the surface in Fourier space. The surface is then multiplied by a Gaussian filter

$$G(k_x) = e^{\frac{k_x^2}{2\sigma^2}}, \tag{2.2}$$

where σ is the width of the Gaussian, that damps out the high frequencies. A characteristic model surface power spectral density is shown in Figure 2.5. An inverse Fourier transform is then done on the filtered surface to obtain the final surface. This process returns a more realistic surface and is done in the surface generation for all calculations we have done. This process can is shown in Figure 2.6. Nethercott *et al.* used GO to give a proof of principle, showing that the reflection could be used to determine the surface roughness of a sample [21].

The PO calculation improves on GO by taking into account the currents that are induced on the surface. I will not derive these equations in this paper, but they can be found in Turley [22] and

Johnson [11]. In PO the currents are calculated from the incident beam using

$$\mathbf{K} = -\hat{\mathbf{n}} \times (\mathbf{E}_1 - \mathbf{E}_2) \tag{2.3}$$

$$\mathbf{J} = \hat{\mathbf{n}} \times (\mathbf{H}_1 - \mathbf{H}_2), \tag{2.4}$$

where the $\hat{\mathbf{n}}$ vector is normal to the surface. The subscript 1 refers the incident side of the surface, and 2 refers to inside the thin film. The assumption is made here that the surface is locally smooth. We also assume that the currents on the surface don't interact with each other. The current is only due to the incident field. The Fresnel coefficients were also taken into account when determining the surface currents. The coefficients for reflection are given by Eqs. 2.5 and 2.6.

$$r_s = \frac{n_1 \sin\theta_i - n_2 \sin\theta_t}{n_1 \sin\theta_i + n_2 \sin\theta_t} \tag{2.5}$$

$$r_p = \frac{n_1 \sin\theta_t - n_2 \sin\theta_i}{n_1 \sin\theta_t + n_2 \sin\theta_i} \tag{2.6}$$

where n_1 and n_2 are the indices of refraction for the material of the incident light and transmitted light respectively, θ_i and θ_t are the incident and transmitted angles respectively, and r_s and r_p are the Fresnel coefficients for s and p polarized light respectively. Figure 2.7 shows the geometry used to derive the Fresnel coefficients. The scattered fields can then be found by solving the Helmholtz equations

$$(\nabla^2 + k^2)\mathbf{E}^s = \nabla\left(\frac{\nabla \cdot \mathbf{J}}{i\omega\varepsilon_0}\right) - i\omega\mu_0\mathbf{J} + \nabla \times \mathbf{K} \tag{2.7}$$

and

$$(\nabla^2 + k^2)\mathbf{H}^s = \nabla\left(\frac{\nabla \cdot \mathbf{K}}{i\omega\mu_0}\right) - i\omega\varepsilon_0\mathbf{K} - \nabla \times \mathbf{J}. \tag{2.8}$$

A Green's function solution gives

$$\mathbf{E}^s = -\frac{\nabla(\nabla \cdot \mathbf{A}) + k^2\mathbf{A}}{i\omega\varepsilon_0} - \nabla \times \mathbf{F} \tag{2.9}$$

and

$$\mathbf{H}^s = -\frac{\nabla(\nabla \cdot \mathbf{F}) + k^2\mathbf{F}}{i\omega\mu_0} + \nabla \times \mathbf{A} \tag{2.10}$$

where

$$\mathbf{A}(\mathbf{x}) = \int_S G(\mathbf{x}, \mathbf{x}')\mathbf{J}(\mathbf{x})' d\mathbf{x}' \tag{2.11}$$

and

$$\mathbf{F}(\mathbf{x}) = \int_S G(\mathbf{x}, \mathbf{x}')\mathbf{K}(\mathbf{x})' d\mathbf{x}' \tag{2.12}$$

and $G(\mathbf{x}, \mathbf{x}')$ is the Green's function given by

$$(\nabla^2 + k^2)G(\mathbf{x}, \mathbf{x}') = -\delta(\mathbf{x} - \mathbf{x}'). \tag{2.13}$$

For s polarization the the expression for the scattered field becomes

$$E_z^s = -kg(\rho)e^{i3\pi/4} \int \exp\{i[kx'(\cos\theta_i - \cos\theta_r) - ky'(\sin\theta_i + \sin\theta_r)]\} \times \left(\sqrt{1 + \left(\frac{dy'}{dx'}\right)^2} \sin\theta_i + \sin\theta_r - \cos\theta_r \frac{dy'}{dx'} \right) dx', \tag{2.14}$$

where $k = \frac{2\pi}{\lambda}$ is the wave number, λ is the wavelength, $g(\rho) = \frac{e^{ik\rho}}{2\sqrt{2\pi k\rho}}$ is a spherical wave a distance ρ from the interface, x' and y' are the coordinates of the surface, and θ_i and θ_r are the angles of incidence and reflection respectively.

We modified the code to vary the incident beam profile to include incident beams other than a plane wave. If a plane wave is used in the calculation the reflection will have bumps on the wings due to diffraction from the edges of the sample. If the incident beam is weak close to the edges of the sample the diffraction effects are small. Figure 2.8 shows the difference in reflection from a flat surface using a plane wave and a Gaussian incident beam.

In the future we will be comparing the physical optics code to an exact calculation using Maxwell's equations. Johnson [11] found that PO and the exact solution did not agree for rough surfaces. Since we are using this analysis to measure roughness the exact solution should be better than PO. This paper shows that reflection measurements can tell us how rough a surface is, however, this analysis should be redone using the exact calculation instead of PO.

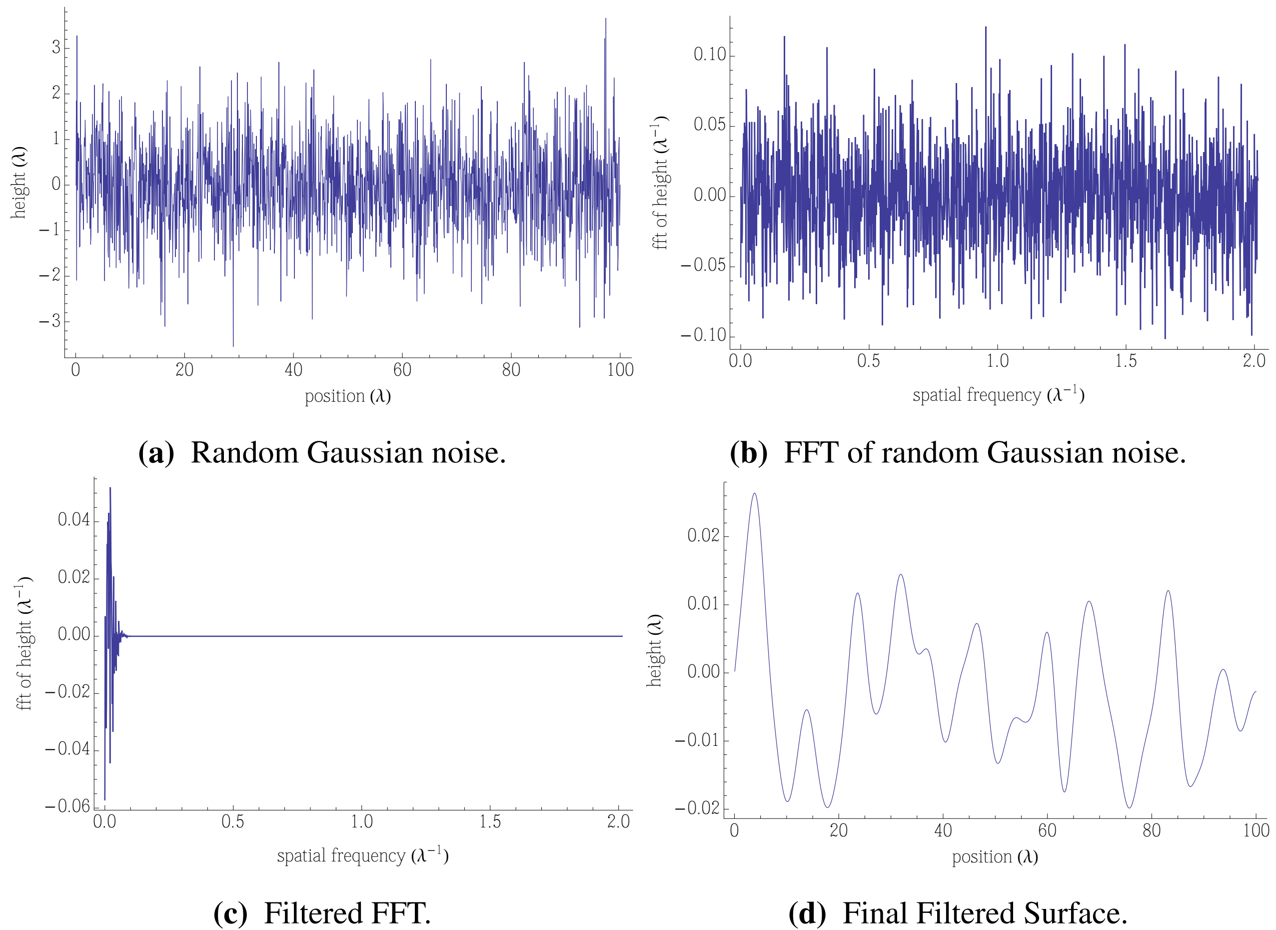

(a) Random Gaussian noise.

(b) FFT of random Gaussian noise.

(c) Filtered FFT.

(d) Final Filtered Surface.

Figure 2.6 This illustrates the model surface creation process from Figures a-d. First random Gaussian noise is generated and then transformed into frequency space. In frequency space the noise is multiplied by a Gaussian to filter out the high frequency components and then transformed back to position space. This surface was generated with a length of 100 λ (wavelengths), and rms height of 0.01 λ, and Gaussian width of 0.1 λ^{-1}.

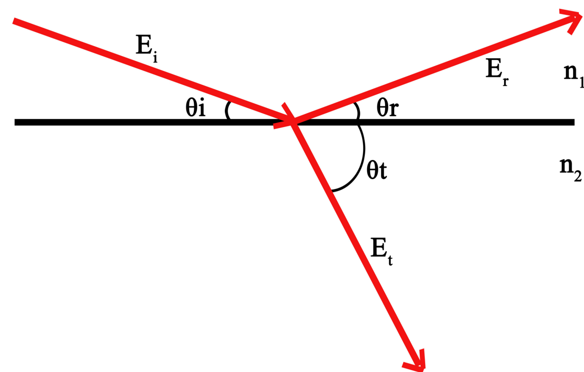

Figure 2.7 Geometry used to derive the Fresnel coefficients.

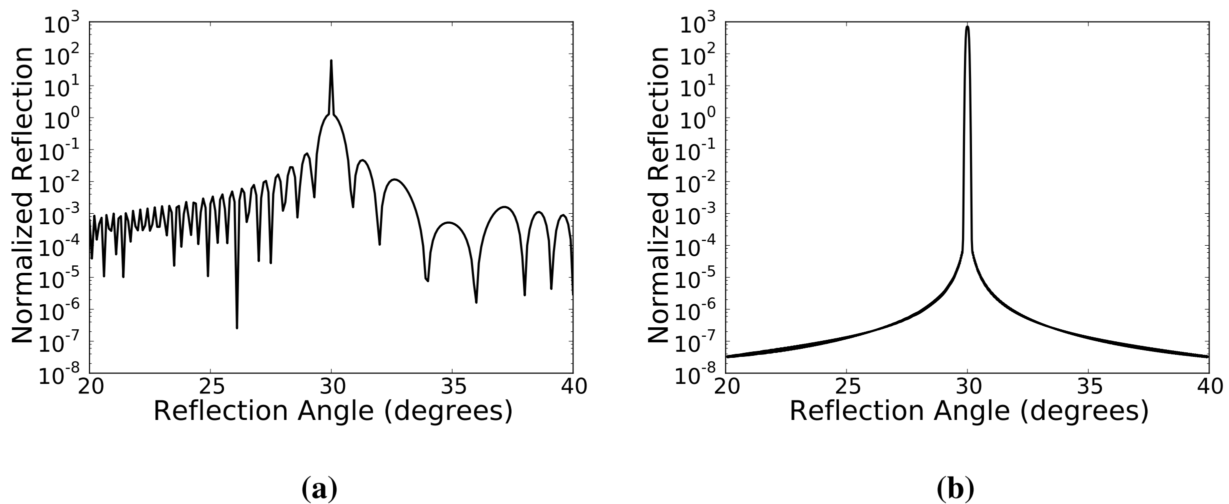

Figure 2.8 Here are reflections from different incident beams. Figure 2.8a is a plane wave with a width of 1000 wavelengths. Figure 2.8b is a Gaussian wave with a width of 4000 wavelengths. The -σ to σ width is 1000 wavelengths. Notice the additional bumps away from the specular peak for the plane wave. This is due to the sharp cutoff of the wave at the edge of the sample. The Gaussian wave is weakest at the edge and thus diffraction effects are minimized.

Chapter 3

Results

3.1 Reflection

The reflection measurements that are reported here were all taken at the ALS. We took four reflection measurements from each sample. The data set that we took are shown in Table 3.1. These measurements are plotted in Figures 3.1 and 3.2 for the 412 and 44 nm samples respectively.

Notice that in Figure 3.1 the shapes of the peaks all looked relatively similar. We were able to determine the roughness from each of these measurements. However notice in Figure 3.2 how sensitive the shape of the reflection of the 44 nm sample is to the wavelength. All three measurements on the 44 nm sample done with 25 nm light showed a very wide central peak. These may have something to do with the large scale bumps on the surface that can be seen in the AFM picture in Figure 2.4.

3.2 Understanding Surface Roughness

By varying the model roughness parameters in our PO code we have determined the roughness of the 412 nm sample. The reflection from the 44 nm sample had a shape that we could not match with

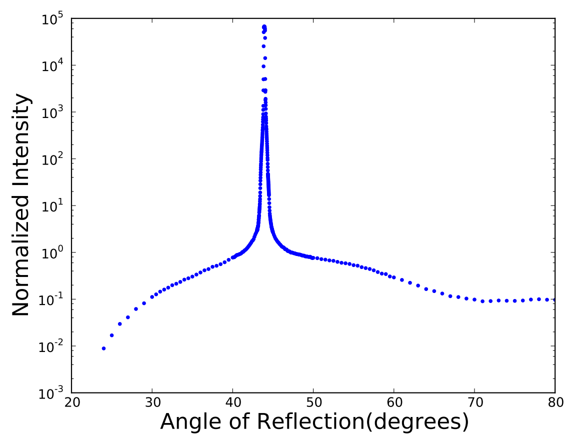

(a) $\lambda = 25$ nm, $\theta = 22^{\circ}$

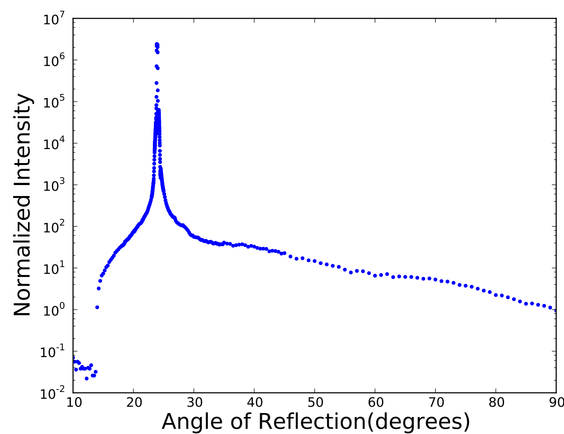

(b) $\lambda = 25$ nm, $\theta = 12^{\circ}$

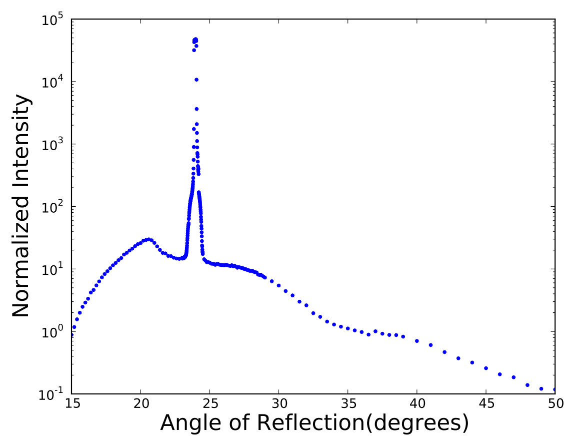

(c) $\lambda = 5$ nm, $\theta = 12^{\circ}$

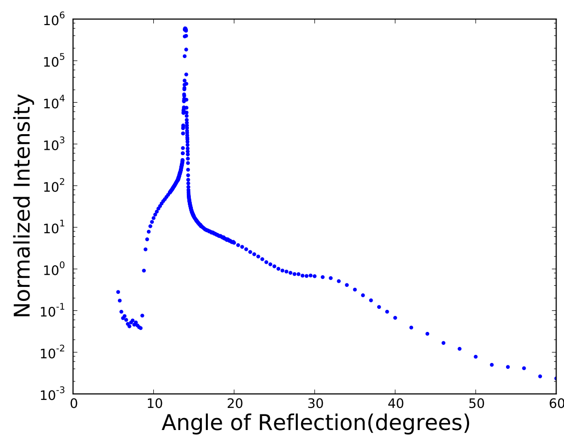

(d) $\lambda = 5$ nm, $\theta = 7^{\circ}$

Figure 3.1 Plots of reflection data for the 412 nm sample. These data are normalized to the measured reflectivity of the sample.

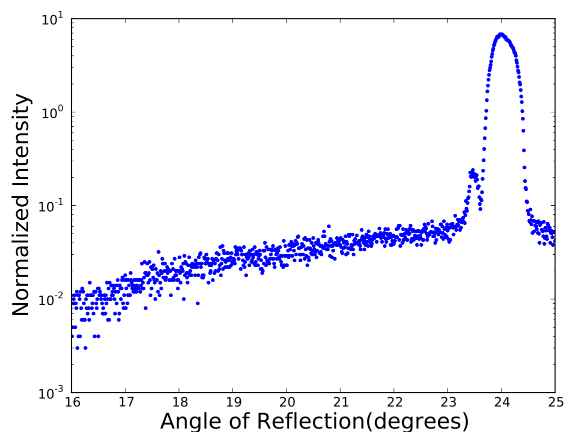

(a) λ = 25 nm, θ = 12°, position = A

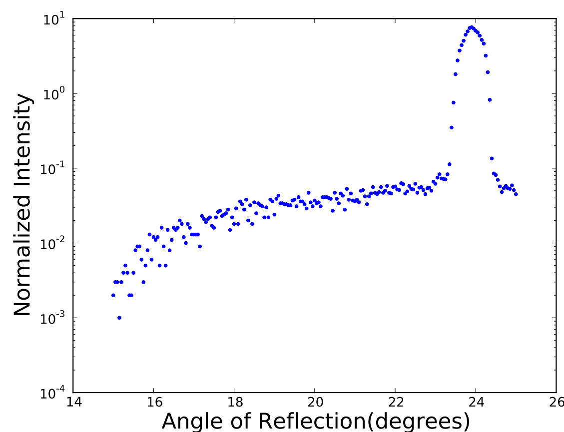

(b) λ = 25 nm, θ = 12°, position = B

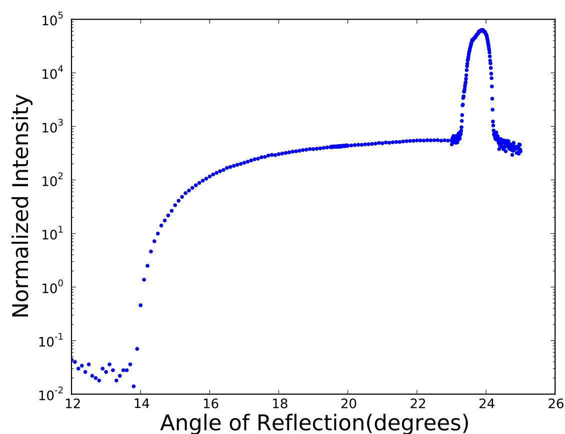

(c) λ = 25 nm, θ = 12°, position = C

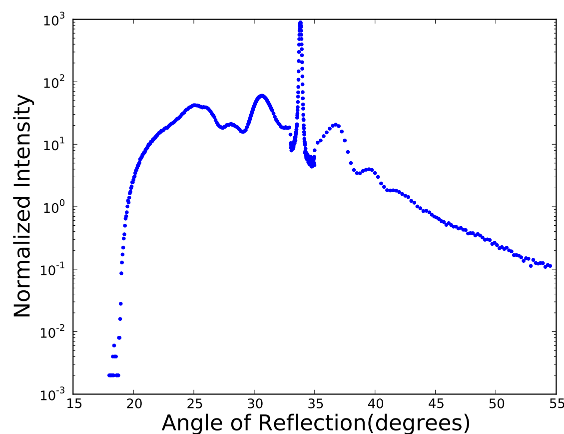

(d) λ = 5 nm, θ = 17°, position = C

Figure 3.2 Plots of reflection data for the 44 nm sample. These data are normalized to the measured reflectivity of the sample. Position A, B and C correspond to rough, less rough, and relatively smooth spots on the sample respectively

Table 3.1 Reflection measurements for two UO_x samples. All data on the 412 nm sample was taken at one points. The positions A, B and C for the 44 nm sample correspond to different positions on the sample, each of varying roughness.

Sample thickness nm	Position	Wavelength nm	Incident Angle degrees
412		25	22
412		25	12
412		5	12
412		5	7
44	A	25	12
44	B	25	12
44	C	25	12
44	C	5	17

our model. We suspect that this is due to the large scale bumps on the surface. The two parameters that we varied were rms roughness height and width of the Gaussian filter. Each parameter had different effects on the reflection. As the rms height increased the peak of the reflection decreased and the wings of the reflection increased. When the width of the Gaussian filter increased the wings grew but the peak remained untouched. Each measurement on the 412 nm sample had a slightly different measurement for the rms height. The rms heights were 0.625±0.050 nm, 0.925±0.175 nm, 0.12±0.015 nm and 0.785±0.045 nm in the order the measurements show up on Table 3.1. If the measurements for Figures 3.1(a,b,d) are averaged the result provides a reasonable fit for all of the measurements. The averaged results give an rms height of 0.78±0.15 nm and a Gaussian cutoff width of 8.3e-5±2.7e-5 nm^{-1}. Plots of the fitted measurements and calculations are shown in Figure 3.3. For each fit the measured data was normalized to one and the peak of the calculated data was forced to match the peak of the calculated data. This way the shapes of the reflection

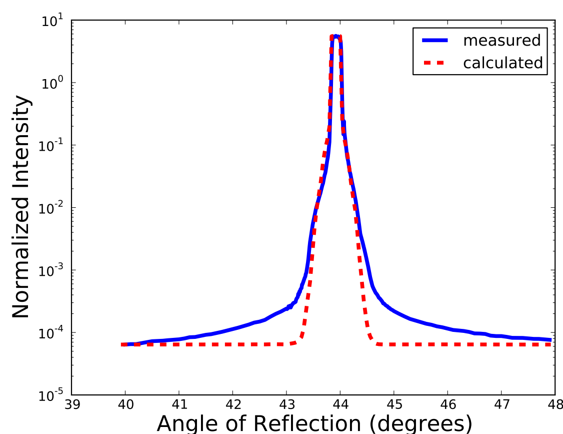

(a) $\lambda = 25$ nm, $\theta = 22^{\circ}$

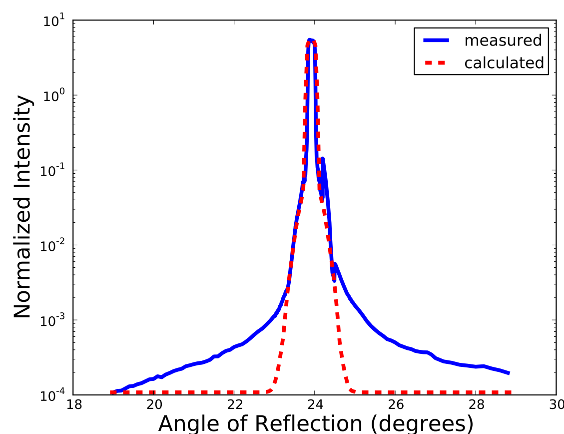

(b) $\lambda = 25$ nm, $\theta = 12^{\circ}$

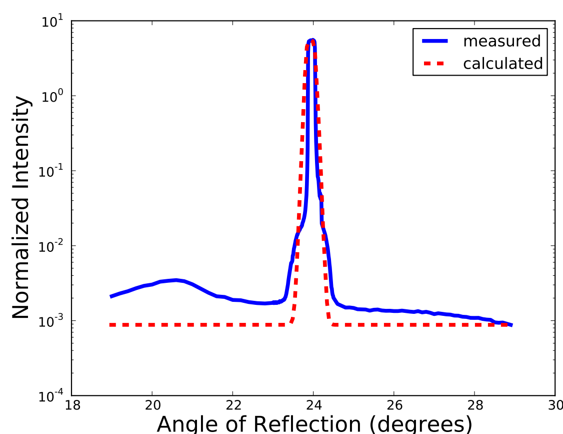

(c) $\lambda = 5$ nm, $\theta = 12^{\circ}$

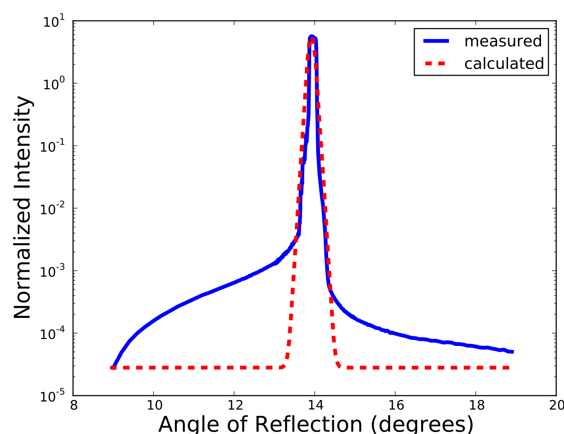

(d) $\lambda = 5$ nm, $\theta = 7^{\circ}$

Figure 3.3 Plots of reflection data for the 412 nm sample compared with its fit to the calculation from a model surface. These plots were all done with the averaged fitting values. The measured calculation was normalized to have an integral of one across the angles plotted. The peak of the calculated reflection was then forced to match the measured peak. This way the central peaks could be compared. The height is in rms height and the width is the width of the Gaussian filter used on the model surface. Both of these parameters are measured in wavelengths.

profiles could be compared. The fits were only valid to within about a degree, which means that we may need a more adjustable surface model. This may also be due to an error in our surface model or background noise in the data that we didn't subtract out. We decided to fit the central peak as a result.

Though we were not able to directly measure the rms height and spatial frequency of the 44 nm sample, we were able to use GO to understand the larger scale, on the order of hundreds of nm in diameter, bumps on the surface as seen in Figure 2.4a from the AFM. Assuming that the bumps on the surface are quadratic, GO predicts that there will be a central peak and then an almost flat, slowly falling off, wing. The wing will fall off quickly to zero as the maximum angle of reflection is reached. If the bumps are described by

$$h(x) = b - \frac{b}{a^2}x^2 \tag{3.1}$$

where $h(x)$ is the function that describes the height of the surface and a and b are the height and radius of the bumps respectively, then the angle that the bump reflects light, θ, is given by

$$\begin{aligned} \theta &= \arctan\left(-h'(x)\right) \\ &= \arctan\left(2\frac{b}{a^2}x\right). \end{aligned} \tag{3.2}$$

The maximum angle of reflection for a quadratic bump would then be given by $\theta_{\text{max}} = \theta(x = a)$ or

$$\theta_{\text{max}} = \arctan\left(2\frac{b}{a}\right). \tag{3.3}$$

This maximum angle would be the angle at which the flat section would fall off. This maximum angle would give a characteristic shape as shown in Figure 3.4. The shape can be seen in Figures 3.2c and 3.2d, except for the extra diffraction bumps in Figure 3.2d. Figures 3.2a and 3.2b look like they probably show this same characteristic shape but we don't have enough data to verify. This angle is indicated in Figure 3.5 for a characteristic reflection curve by the red vertical lines.

Though this method gave us a good qualitative understanding into reflection from surfaces with

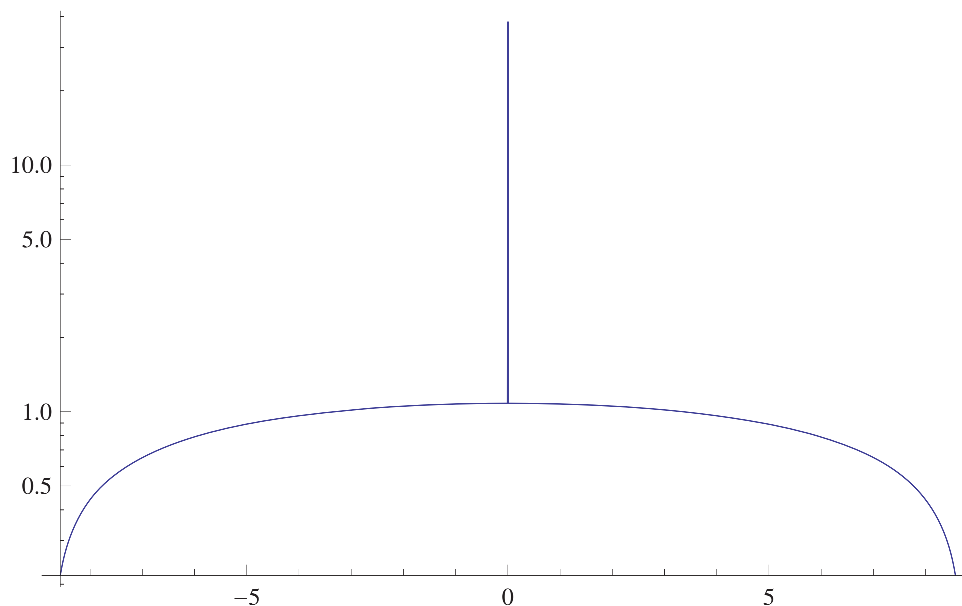

Figure 3.4 Characteristic curve predicted by GO for a bumpy surface. The ratio of radius to height of these bumps was 13 which gave a maximum angle of 8.7°

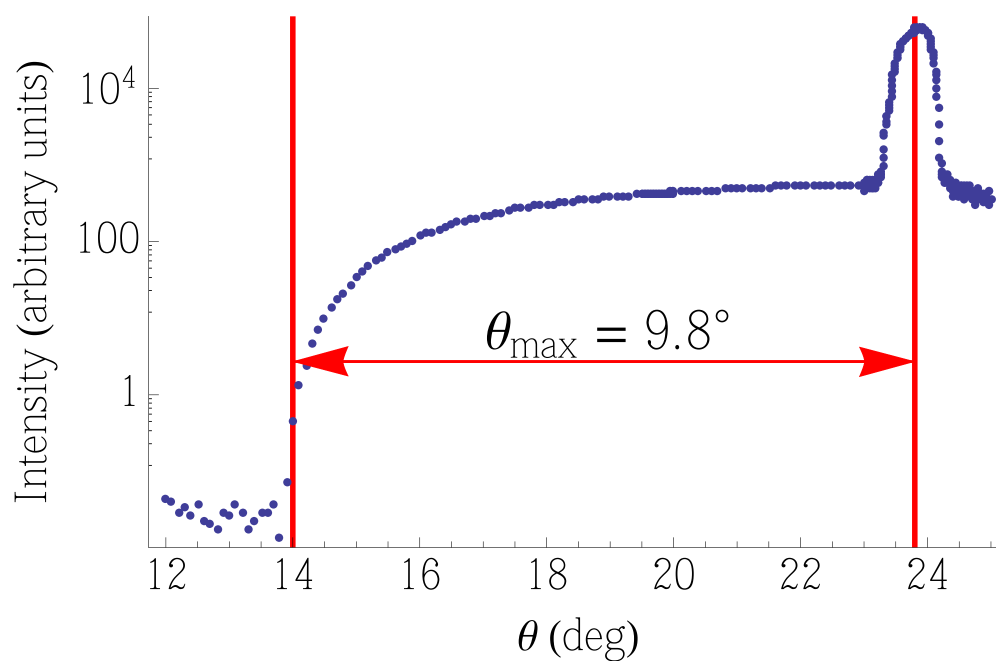

Figure 3.5 Red vertical line shows the maximum angle of reflection. A maximum angle of reflection is predicted by GO.

bumps, there was quantitative disagreements. For example, Figure 3.5 had $\theta_{\max} \approx 9.8^\circ$ while the AFM showed that the bumps on the 44 nm sample had $\frac{b}{a} \approx \frac{1}{3}$ giving us a $\theta_{\max} \approx 33.7^\circ$.

3.3 Comparison to AFM

The AFM measurements gave us initial insight into our surface but didn't provide the resolution that we hoped to achieve with our method. With the AFM we determined the rms roughness heights of the 412 and 44 nm samples to be 9.39 and 16.8 nm respectively. These values don't match the values that we determined using our method, which we expected. At some point a sample is too smooth for AFM to give precise measurements. It is at this point that our method can take over.

Chapter 4

Conclusion

4.1 Conclusion

We have developed a method for determining the roughness of a thin film based on its reflection profile. Though we were not able to determine the roughness of both UO_x thin films, we were able to show that this method is valid, if a good surface model is used. For the 44 nm sample a different model needs to be used for the surface. For the 412 nm sample four measurements were taken at different incident angles and with different wavelengths of light. By fitting these reflection measurements to PO calculations with model surfaces we were able to determine the rms roughness to be 0.78±0.15 nm and the Gaussian filter width to be $8.3 \times 10^{-5} \pm 2.7 \times 10^{-5}\,\text{nm}^{-1}$. This is different than the predicted values of the AFM which reported an rms roughness height of 9.39 nm for the 412 nm sample. Our measurement has more resolution that the AFM because of the small wavelength of EUV light.

4.2 Future Work

This method will be improved in the future by using exact boundary element calculations to compare the reflection measurements as opposed to the PO calculation that we use here [11]. We will also be improving our surface model to better fit our surfaces. In addition we would like to also take measurements at BYU to compare with those from the ALS. Currently BYU uses a helium plasma hollow cathode EUV source, designed after the reflectometer in by Peresce *et al*. [23]. In the future we hope to compare these ALS measurements with those taken at BYU. The reflectometer at BYU does not have access to as many wavelengths of light as the ALS, nor is the beam as bright as the beam at the ALS. However, being able to take these measurements locally would be more convenient. Also, at BYU we could make iterative measurements with more samples and watch surface features change under various growth, annealing, and deposition processes. To better understand the connection between surface roughness and reflection we will also be taking more measurements on a variety of thin films.

Bibliography

[1] B. Sandel *et al.*, “The Extreme Ultraviolet Imager Investigation for the IMAGE Mission,” Space Science Reviews **91,** 197–242 (2000).

[2] C. Wagner and N. Harned, “EUV lithography: Lithography gets extreme,” Nature Photonics **4,** 24–26 (2010).

[3] U. Feldman, P. Mandelbaum, J. F. Seely, G. A. Doschek, and H. Gursky, “The portential for plasma diagnostics from stellar extreme-ultraviolet observations,” Astrophys. J. Suppl. Ser. **81,** 387–408 (1992).

[4] D. E. Savage, J. Kleiner, N. Schimke, Y. H. Phang, T. Jankowski, J. Jacobs, R. Kariotis, and M. G. Lagally, “Determination of roughness correlations in multilayer films for xray mirrors,” J. Appl. Phys. **69,** 1411 (1991).

[5] K. L. Westra and D. J. Thomson, “Effect of tip shape on surface roughness measurements from atomic force microscopy images of thin films,” J. Vac. Sci. Technol. B **13,** 344 (1995).

[6] W. T. Doughty, “Roughness Correction Model for Reflection From Perfectly Conducting Scatterers,” Brighan Young University (2008), Senior Thesis.

[7] G. Hart, “Correcting for Reflection Attenuation in the Extreme Ultraviolet due to Surface Roughness,” Brigham Young University (2012), Senior Thesis.

[8] P. Debye, “Interferenz von Röntgenstrahlen und Wärmebewegung,” Annalen der Physik **348,** 49–92 (1913).

[9] I. Waller, “Zur Frage der Einwirkung der Wärmebewegung auf die Interferenz von Röntgenstrahlen,” Zeitschrift fur Physik **17,** 398–408 (1923).

[10] P. Croce and L. Névot, “Étude des souches minces et des surfaces par réflexion rasante, spéculaire ou diffuse, de rayons X,” Rev. Phys. Appl. (Paris) **11,** 113–125 (1976).

[11] J. E. J. Johnson, Master’s thesis, Brigham Young University, 2006.

[12] D. G. Stearns, “The scattering of x rays from nonideal multilayer structures,” J. Appl. Phys. **65,** 491 (1989).

[13] L. G. Parratt, “Surface Studies of Solids by Total Reflection of X-Rays,” Phys. Rev. **95,** 359 (1954).

[14] S. K. Sinha, E. B. Sirota, and S. Garoff, “X-ray and neutron scattering from rough surfaces,” Phys. Rev. B **38,** 2297–2312 (1988).

[15] E. M. Gullikson, “Scattering from normal incidence EUV optics,” SPIE **3331,** 72–80 (1998).

[16] D. D. Allred, Private Communication, 11 Jul 2014.

[17] R. L. Sandberg, D. D. Allred, L. J. Bissell, J. E. Johnson, and R. S. Turley, “Uranium Oxide as a Highly Reflective Coating for 100-400 eV,” In *AIP Conference Proceedings*, **705,** 796 (San Francisco, 2004).

[18] J. W. Bell, “Thickness Uniformity of Uranium Oxide Films Sputtered While Undergoing Planetary Motion,” Brigham Young University (2013), Senior Thesis.

[19] “The Center for X-Ray Optics,”, http://www.cxro.lbl.gov/reflectometer, accessed: 2014-07-15.

[20] J. H. Underwood, E. M. Gullikson, M. Koike, P. J. Batson, P. E. Denham, K. D. Franck, R. E. Tackaberry, and W. F. Steele, “Calibration and standards beamline 6.3.2 at the Advanced Light Source,” Rev. Sci. Instrum. **67,** 3373 (1996).

[21] Q. Nethercott, C. L. Petrie, and R. S. Turley, “Non-specular Reflectance in the Extreme Ultraviolet,” Utah Academy of Sciences, Arts, and Letters **89,** 181–193 (2012).

[22] R. S. Turley, “Physical Optics,”, BYU Internal Report, 2013.

[23] F. Peresce, S. Kumar, and C. S. Bowyer, “Continuous Discharge Line Source for the Extreme Ultraviolet,” Appl. Opt. **10,** 1904 (1971).

Index

Advanced Light Source, 13
Atomic Force Microscopy, 4, 16

BYU Reflectometer, 32

DC Magnetron Sputtering, 13
Debye-Waller, 6

Electron Microscopy, 5

Geometrical Optics, 7, 18

IMAGE mission, 1

Lithography, 1

Maxwell's equations, 20
Multilayer mirrors, 3

Nevot-Croce, 6

Physical Optics, 8, 18